Advances in Geo-Energy Research

Vol. 18, No. 3, p. 242-256, 2025

Original article

Pressure heterogeneity caused by fluid injection and diffusion controls occurrence of induced earthquakes

Shaobo Han[1], Xiaoying Zhuang[1]*, Qianlong Zhou[2], Wei Feng[3], Xiaodong Hu[2]*, Quanzhou Yao[1]

[1]*Department of Mathematics and Physics, Leibniz University Hannover, Hannover 30167, Germany*

[2]*Unconventional Petroleum Research Institute, China University of Petroleum, Beijing 102249, P. R. China*

[3]*Department of Geosciences, University of Padua, Padua 35131, Italy*

Keywords:
Fluid injection
pressure heterogeneity
heterogeneity threshold
fault stability
rate-and-state friction model

Cited as:
Han, S., Zhuang, X., Zhou, Q., Feng, X., Hu, X., Yao, Q. Pressure heterogeneity caused by fluid injection and diffusion controls occurrence of induced earthquakes. Advances in Geo-Energy Research, 2025, 18(3): 242-256.
https://doi.org/10.46690/ager.2025.12.04

Abstract:
Underground fluid-injection operations, such as hydraulic fracturing and enhanced geothermal stimulation, have triggered multiple earthquakes across the globe. Earthquake nucleation models within the rate-and-state friction framework suggest that an increase in fluid pressure favors stable slip. However, certain observations indicate that fluid injected into faults may reduce effective normal stress, promoting fault failure, which highlights the debate on the role of fluids in controlling earthquake fault stability. This paper proposes a rate-and-state friction-based model of earthquake nucleation that incorporates fluid injection and diffusion processes, and extends the stability criteria of the system. The results show that fluid pressure heterogeneity can indeed influence fault stability. Elevated fluid pressure stabilizes faults, however, fluid pressure heterogeneity counteracts this stabilizing effect. The model suggests that pressure heterogeneity above a certain threshold facilitates seismic slip, whereas heterogeneity below this threshold can stabilize it. The results further indicate that this threshold reflects a universal instability criterion inherent to the system, rather than an incidental product of a specific fault or rock type. Accordingly, this study proposes a pressure-heterogeneity index as an operational precursor: Tracking spatiotemporal pore-pressure heterogeneity can guide the traffic-light-style adaptive control of injection. These insights provide a new, mechanism-based explanation for the role of fluids in triggering earthquakes.

1. Introduction

Seismic activities induced by underground fluid injection for hydraulic stimulation and enhanced geothermal systems usually occur in fault regions associated with elevated pore fluid pressure (Ito et al., 2013; Anyim and Gan, 2020; Hui et al., 2022; Jiang et al., 2025). According to the classical effective stress law and Mohr-Coulomb framework, slip occurs when shear stress exceeds strength (Hubbert and Rubey, 1959; Atkinson et al., 2020; Sun et al., 2024). It is apparent that elevated pore pressure can reduce effective normal stress and promote fault slip (Zhu et al., 2020; Feng et al., 2023, 2024; Song et al., 2024). Some studies have shown that high fluid pressure leads to unstable sliding (Ellsworth, 2013; Scuderi and Collettini, 2016). However, earthquake nucleation models based on the rate-and-state friction (RSF) framework show the fault slip at decreased normal stress (equivalent to an increase in fluid pressure) favors stable sliding and aseismicity, contrary to the observed increases in seismicity that is usually attributed to fluid injection (Dieterich, 1978; Ikari et al., 2013). Although attempts have been made to evaluate this argument using the creep experiment (Bos and Spiers, 2002), this approach also has yielded the opposite results with respect to RSF. Notably, experimental observations have also shown that an increase in

Yandy Scientific Press

*Corresponding author.
E-mail address: shaobohan@iop.uni-hannover.de (S. Han); zhuang@iop.uni-hannover.de (X. Zhuang); 2021216583@student.cup.edu.cn (Q. Zhou); wei.feng@unipd.it (W. Feng); huxiaodong@cup.edu.cn (X. Hu); yaoqz@sustech.edu.cn (Q. Yao).

Received September 29, 2025; revised October 24, 2025; accepted November 11, 2025; available online November 15, 2025.

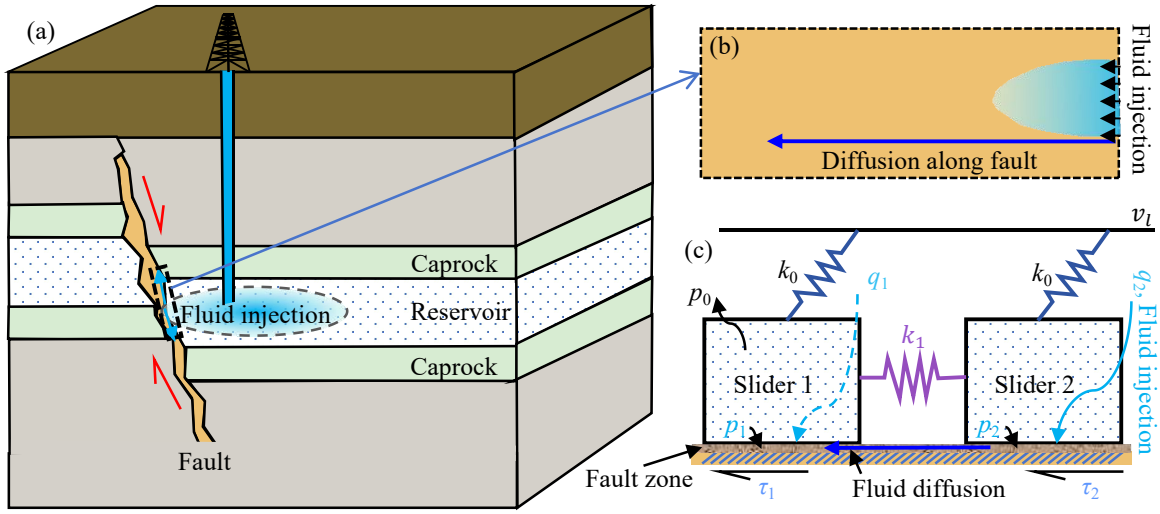

Fig. 1. Schematic diagram of fluid injection and diffusion: (a) Conceptual image of induced seismicity, (b) enlarged view of fluid injection and diffusion in (a), and (c) the mechanical conceptual image of the spring-slider model.

pore pressure stabilizes fault slip (Bedford et al., 2021; Zega and Zhu, 2023). Given these conflicts between the effective stress law and earthquake nucleation models, the role of fluid pressure in controlling fault stability remains enigmatic.

The RSF framework has been widely used to model fault slip for both induced and natural earthquakes. Within the RSF framework, fault stability is governed by the competition between the system's stiffness and the critical stiffness (Dieterich, 1978). Under pore-pressure elevation, the critical stiffness decreases, which shows that elevated fluid pressure stabilizes fault slip rather than triggers earthquakes (Scholz, 1998; Ikari et al., 2013; Cappa et al., 2019; Sun et al., 2024) or supports the late stabilization of the fault (Alghannam and Juanes, 2020). Nevertheless, this stabilizing prediction is inconsistent with observations of increased seismicity and dynamic slip during fluid injection (Sawai et al., 2016; Scuderi et al., 2017). A major limitation of most existing studies is that they treat pore pressure as spatially uniform or quasi-uniform, without explicitly accounting for fluid injection, diffusion, and the resulting along-fault pore pressure heterogeneity. Recent studies indicate that fluid diffusion and pressure distribution can strongly influence earthquake nucleation and triggering (Cebry and McLaskey, 2021; Gunatilake and Miller, 2025; Liu et al., 2025), yet a quantitative nucleation framework that incorporates the spatial distribution of pore pressure into RSF theory and clarifies its impact on fault stability is still lacking.

In this paper, to account for fluid injection and diffusion, a two-degree-of-freedom spring-slider model of seismic slip based on the rate-and-state friction (RSF) framework is developed. The model shows that the stability of faults is controlled by both fluid injection and diffusion along the fault. The results suggest that high fluid pressure stabilizes or destabilizes earthquake faults depending critically on the fluid pressure distribution along the fault. In qualitative terms, this finding is consistent with experimental observations conducted on shale fault gouge (Scuderi and Collettini, 2018) and polymethyl methacrylate (PMMA) (Cebry and McLaskey, 2021) and may also explain observations of fluid pressure stabilizing or destabilizing subduction zone faults (Sawai et al., 2016; Tarling et al., 2019).

2. Model and methods

After being injected into the fault, fluid diffuses along the fault plane, resulting in a spatially heterogeneous pore-pressure distribution (Figs. 1(a) and 1(b)). To simulate the effects of this process on fault slip, a two-degree-of-freedom spring-slider model that incorporates fluid injection and diffusion was developed (Fig. 1(c)). The model consists of two sliders labeled $i = 1,\ 2$, respectively. Each slider is connected by a coupling spring with stiffness k_1 and pulled by a loading spring with stiffness k_0. The ends of these loading springs are constrained to move at a constant slip velocity v_l. Here, the fluid injection approach is used to create high pore pressures in the fault zones containing low-permeability cores; q_i denotes the injection rate. The entire fault is homogeneous, including the hydraulic properties along the fault. The pressure at the bottom of the slider is denoted as p_i, and the ambient pressure as p_0.

2.1 Governing equations

According to Newton's second law, the equation of motion in the horizontal direction along the strike can be written as (Burridge and Knopoff, 1967):

$$m_i\ddot{x}_i = k_0 u_i^* + k_1 u_i - k_1 u_{i-1} - \tau_i, \quad i = 1,2 \tag{1}$$

where the double dot over x_i (i.e., $\ddot{x}_i$) represents the second-order derivative with respect to time, x_i represents the position coordinates of each slider, m_i represents the mass of the slider, k_0 represents the loading spring stiffness, k_1 represents the coupling stiffness, $u_i^* = v_l t - x_i$ is the relative displacement between loading point and i-th slider, $u_i = x_{i+1} - x_i$ is the relative displacement between $(i+1)$-th and i-th slider, and $u_{i-1} = x_i - x_{i-1}$ is the relative displacement between i-th and $(i-1)$-th slider. Here, $x_0 = x_1$ and $x_{N+1} = x_N$ $(N = 2)$

are considered, N is the number of sliders. Furthermore, $\tau_i(=\mu\sigma_i',\ \mu=\mu_*+a_i\ln(v_i/v^*)+\theta_i,\ \sigma_i'=\sigma-p_i)$ represents the shear stress of each slider, where μ denotes the frictional coefficient, μ_* denotes the constant appropriate for steady-state at normalizing velocity v^*, a_i denotes the "direct-effect" derived from friction experiments, θ_i denotes the state variable, v_i denotes the slip velocity, σ_i' denotes the effective normal stress, σ denotes the normal stress, p_i denotes the pressure at the bottom of the slider, and v_l is the constant loading velocity.

This study adopts the rate-and-state evolution model proposed by Linker and Dieterich (1992), which accounts for the effect of normal stress on the state variable θ_i. Meanwhile, the magnitude of the sudden change is modeled as $\alpha\dot{\sigma}_i'/\sigma_i'$. Here, the state evolution law incorporating the effective normal stress is as follows:

$$\dot{\theta}_i=-\frac{v_i}{d_c}\left(\theta_i+b_i\ln\frac{v_i}{v^*}\right)-\alpha\frac{\dot{\sigma}_i'}{\sigma_i'},\ i=1,\ 2 \tag{2}$$

where the single dot over θ_i (i.e., $\dot{\theta}_i$) represents the first-order derivative with respect to time, d_c denotes the characteristic slip distance, b_i denotes the constitutive parameter, and α is the scaling parameter. Previous studies have shown that α ranges from 0 to μ (Linker and Dieterich, 1992).

The fluid is injected into the fault zone (the brown permeable layer below the slider in Fig. 1(c)) at slider 2 (solid light-blue arrow). Subsequently, the fluid diffuses along the fault-strike direction, from slider 2 to slider 1 (solid blue arrow). The entire fault zone is assumed to be homogeneous, so the parameters of sliders 1 and 2 are the same (i.e., $a_1=a_2=a,\ b_1=b_2=b$). To describe the evolution of pressure and effective stress in the fault zone, this model is coupled with a model of fluid pressure and rock deformation. The source term for fluid injection is $q_2\Delta t$, where q_2 is the fluid injection rate at slider 2, and Δt denotes the time interval. The fluid mass change due to the fluid diffusion is $\Delta m(=-\rho\kappa A(p_2-p_0)\Delta t/\eta L)$, where ρ denotes fluid density, p_2 denotes the pressure at the bottom of the slider 2, p_0 denotes the ambient pressure, κ denotes the rock permeability at injection site, A denotes the basement area (unit area) of the slider, η denotes the fluid viscosity, and L is the characteristic fluid or pressure diffusion length. The mass accumulation term due to fluid injection or rock deformation is $\partial(\rho V_b)\Delta t/\partial t$, where V_b represents the volume of rock. In this model, the injected fluid is assumed to be incompressible, whereas the rock is compressible (Biot, 1941; Wang, 2000; Zhang et al., 2016). The law of mass conservation leads to:

$$\frac{\partial(\rho V_b)}{\partial t}\Delta t-q_2\Delta t=-\frac{\rho\kappa A(p_2-p_0)}{\eta L}\Delta t \tag{3}$$

Furthermore, the mass accumulation term can be expressed as $[\partial(\rho V_b)/\partial t]\Delta t=\rho\,(\partial V(p_2)/\partial t)\Delta t$, where $V(p_2)=V_0[1+\beta(p_2-p_0)]$, V_0 denotes the initial volume of rock, and β is the rock compression coefficient. Therefore, the pore pressure at injection site is given by:

$$\dot{p}_2=c\,(p_0-p_2)+lq_2 \tag{4}$$

where $c=\kappa A/\eta LV_0\beta$ is the diffusion coefficient, and $l=1/\rho V_0\beta$ is the constant parameter. At this point, the trend of fluid pressure change is rapid increase in the early stage and stabilization in the later stage. The fluid diffuses along the strike from the injection point, causing changes in pore pressure in other parts along the fault. During pore pressure diffusion, the spring-slider system is coupled with the fluid diffusion process, and the fluid diffusion equation is discretized using a finite-difference approximation of the Laplace operator to describe the diffusion of fluid pressure between sliders. The resulting discrete form provides a numerical approximation for this rate of change of pore pressure, and the formula is:

$$\frac{\partial p_i}{\partial t}\approx c\,(p_{i-1}-2p_i+p_{i+1}) \tag{5}$$

This expression indicates that the rate of pressure change at slider i not only depends on the current pressure p_i but also on the pressure differences between the neighboring sliders $i-1$ and $i+1$. Considering the Neumann boundary condition ($p_{i-1}=p_i$, i=1), Eq. (5) becomes:

$$\frac{\partial p_1}{\partial t}\approx c\,(p_2-p_1) \tag{6}$$

where p_1 represents the pressure at the bottom of the slider 1. Accordingly, the pore pressure at the diffusion point (slider 1) along strike is given by:

$$\dot{p}_1\approx c\,(p_2-p_1) \tag{7}$$

The pressure changes induced by diffusion influence the effective normal stress on the sliders, which in turn couples with their frictional behavior. By iteratively updating the pore pressure, the motion of sliders becomes interconnected. The discretized diffusion equation thus provides a framework to link the slider dynamics with the spatial distribution of pore pressure. As a result, although the connected springs themselves are local, the pore pressure diffusion introduces an indirect form of long-range interaction, enhancing the physical realism of the system.

These coupled nonlinear ordinary differential equations are solved in MATLAB using the ode15s solver. To understand the influence of fluid injection and diffusion on fault stability, the simulation under the initial conditions detailed in Eqs. (8)-(11) is performed. The model parameters are listed in Table 1. To demonstrate localized slip characteristics, the two-degree-of-freedom spring-slider equations are also formulated. To mitigate potential instabilities and reduce the effects of chaotic behavior inherent to the connected spring model, a parameter setting of $k_0/k_1=1$ is adopted. The simulation results in this study show a slip pattern similar to the B-pattern (periodic oscillation) in the study of Abe and Kato (2013) (Fig. 2). This choice effectively avoids the occurrence of chaotic behavior. The initial conditions are as follows:

$$u_i(t=0)=\left[\mu_*+(a-b)\ln\frac{v_0}{v_*}\right]\frac{(\sigma-p_0)}{k_0} \tag{8}$$

$$v_i(t=0)=v_l \tag{9}$$

$$\theta_i(t=0)=\frac{d_c}{v_l} \tag{10}$$

$$p_i(t=0)=p_0 \tag{11}$$

where $i=1,\ 2$, $b-a=0.01$, v_0 denotes the initial slip velocity.

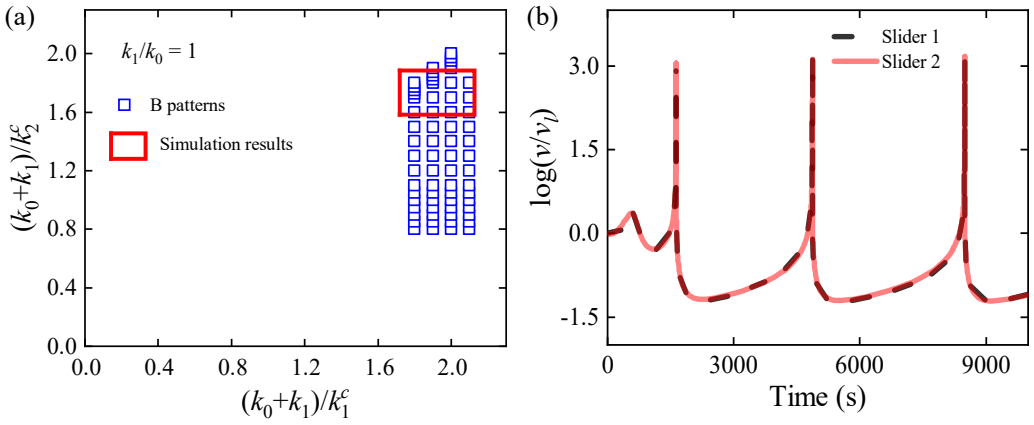

Fig. 2. Classification of slip patterns of the simulation results: (a) Phase diagrams of slip patterns and (b) example simulated histories of velocity.

Table 1. Parameter values for the model.

Parameters	Value
Reference slip rate (m/s)	0.00045
Reference frictional coefficient (-)	0.7
Normal stress (MPa)	100
Ambient pressure (MPa)	50
Fluid injection rate (kg/s)	0.001 *
Characteristic slip distance (m)	0.081
Proportional parameter (-)	1
Constant parameter (MPa/kg)	1.5625
Spring stiffness ratio (-)	1
Diffusion coefficient (1/s)	0.001 *
"Direct-effect" parameter (-)	0.01
Constitutive parameter(-)	0.02
Fluid diffusion site (-)	Slider 1
Fluid injection site (-)	Slider 2

Notes: The superscript * represents that values are varied in the parameter space study.

2.2 Moment magnitude

The moment magnitude (M_w) is a widely used characteristic to describe the magnitude of an earthquake. The following equations are used to calculate the moment magnitude of the slip event for each fluid injection plan (Zhu et al., 2021):

$$E_s = \Delta\tau_{1/4}\Delta\delta A \tag{12}$$

$$\log_{10} E_s = 1.5M_w + 4.8 \tag{13}$$

where E_s represents the total radiated seismic energy, M_w denotes the moment magnitude, $\Delta\tau_{1/4}$ is equal to 1/4 of the stress drop $\Delta\tau$, and $\Delta\delta$ is incremental fault slip. This study takes 1/4 of the dynamic stress drop as the required stress drop and uses the dynamic slip as the incremental fault slip when calculating the moment magnitude.

2.3 Extension of system stability conditions

If the rate at which the frictional resistance of the system changes with sliding exceeds the rate the system can sustain, the system will undergo unstable stick-slip (Linker and Dieterich, 1992; Byerlee, 1970; Ruina, 1983). Here, the quasi-steady-state approximation is employed to freeze time in the pore pressure solution, and a linear stability analysis of the two-degree-of-freedom spring-slider model is performed at a fixed pore pressure (Rao and Arkin, 2003; Alghannam and Juanes, 2020). In addition, the fluid diffused to each slider is assumed as a "virtual" fluid injected directly from the slider (dashed line in Fig. 1(c)). Therefore, this system is simplified to a discrete unit model, where the slider of each unit has independent fluid injection. The quasi-static motion equation of the spring-slider system at variable pore pressure p_i is given as follows:

$$\dot{u}_i^* = v_l - v_i \tag{14}$$

$$0 = k_0 u_i^* - \left(\mu_* + a\ln\frac{v_i}{v^*} + \theta_i\right)(\sigma - p_i) \tag{15}$$

$$\dot{\theta}_i = -\frac{v_i}{d_c}\left(\theta_i + b\ln\frac{v_i}{v^*}\right) - \alpha\frac{\dot{\sigma}_i'}{\sigma_i'} \tag{16}$$

Then, by linearizing Eqs. (14)-(16) about the quasi-steady-state and taking the time derivative of Eq. (15), we can obtain:

$$\Delta\dot{v}_i = \frac{v_0}{a}\left[-\frac{\alpha}{v_0}\frac{(\dot{\sigma} - \dot{p}_i)}{\sigma - p_i} + \frac{b}{d_c} - \frac{k_0}{\sigma - p_i}\right]\Delta v_i + \frac{v_0^2}{ad_c}\Delta\theta_i \tag{17}$$

$$\Delta\dot{\theta}_i = \left[\frac{\alpha}{v_0}\frac{(\dot{\sigma} - \dot{p}_i)}{\sigma - p_i} - \frac{b}{d_c}\right]\Delta v_i - \frac{v_0}{d_c}\Delta\theta_i \tag{18}$$

Eqs. (17) and (18) represent a 2×2 autonomous system of linear ordinary differential equations with solutions of the form $\Delta v_i = V_i e^{\lambda t}$, $\Delta\theta_i = \Theta_i e^{\lambda t}$, where λ represents the growth rate and t is time. Substituting these forms into Eqs. (17) and (18) results in the following characteristic equation:

$$ad_c(\sigma - p_i)\lambda^2 + [v_0(\sigma - p_i)(a-b) - ad_c\dot{p}_i + v_0 d_c k_0]\lambda + k_0 v_0^2 = 0 \tag{19}$$

If the real part of the roots λ_i is negative for all i values, the perturbation of each slider is damped, so this single-degree-of-freedom spring-slider system is stable. On the contrary, if the

real part of the roots λ_i is positive for some i, the perturbation of each slider grows exponentially, so this system is unstable. When the real part of the roots λ_i is zero, the critical stiffness $k_{0,i}^c$ of the loading system of each spring-slider will be:

$$k_{0,i}^c = \frac{(b-a)(\sigma - p_i)}{d_c} - \frac{\alpha}{v_0}\dot{\sigma}_i' \tag{20}$$

The critical stiffness of this model consists of injection term and diffusion term, which are as follows:

Injection site:

$$k_{0,2}^c = \frac{(b-a)(\sigma - p_2)}{d_c} + \frac{\alpha}{v_0}[c(p_0 - p_2) + lq_2] \tag{21}$$

where l is a constant, and p_2 is the fluid pressure at the injection point.

Diffusion site:

$$k_{0,1}^c = \frac{(b-a)(\sigma - p_1)}{d_c} + \frac{\alpha}{v_0}[c(p_2 - p_1)] \tag{22}$$

Following the stability theory of multi-degree-of-freedom systems, the total critical stiffness k_0^c can be described using a modal weighting method (considering a first-order approximation):

$$k_0^c \approx \frac{\langle \mathbf{u}^*, \mathbf{k}_2 \rangle + \langle \mathbf{u}^*, \mathbf{k}_1 \rangle}{\|\mathbf{u}^*\|_2} \tag{23}$$

where $\mathbf{u}^* = [u_1^*, u_2^*, \cdots, u_N^*]^T$ is critical mode displacement vector; $\mathbf{k}_2 = \left[0, 0, \cdots, 0, k_{0,2}^c\right]^T$ is injection effect vector; $\mathbf{k}_1 = \left[k_{0,1}^c, 0, \cdots, 0\right]^T$ is diffusion effect vector; $\langle \cdot, \cdot \rangle$ is Euclidean inner product; $\| \cdot \|_2$ is Euclidean norm.

The inner product term is expanded as:

$$\langle \mathbf{u}^*, \mathbf{k}_2 \rangle = k_{0,2}^c u_2^* \tag{24}$$

$$\langle \mathbf{u}^*, \mathbf{k}_1 \rangle = k_{0,1}^c u_1^* \tag{25}$$

$$\|\mathbf{u}^*\|_2 = \sqrt{\sum_{i=1}^{2} u_i^{*2}} \tag{26}$$

Then, Eq. (23) is substituted to obtain:

$$k_0^c \approx \frac{k_{0,2}^c u_2^* + k_{0,1}^c u_1^*}{\sqrt{\sum_{i=1}^{2} u_i^{*2}}} \tag{27}$$

Finally, the approximate critical stiffness of the whole system is derived as:

$$k_0^c \approx \frac{\left\{\frac{(b-a)(\sigma - p_2)}{d_c} + \frac{\alpha}{v_0}[c(p_0 - p_2) + lq_2]\right\} u_2^* + \left\{\frac{(b-a)(\sigma - p_1)}{d_c} + \frac{\alpha}{v_0}[c(p_2 - p_1)]\right\} u_1^*}{\sqrt{\sum_{i=1}^{2} u_i^{*2}}} \tag{28}$$

where $\sqrt{\sum_{i=1}^{N} u_i^{*2}}$ denotes effective displacement, and this displacement can reflect the comprehensive characteristics of the system. When the shear stiffness of the loading system is less than a critical value given by Eq. (28), the motion of the system is unstable; conversely, the system moves to a stable state.

The validation of the approximate solution expression for the critical stiffness mentioned above is conducted in MATLAB. The quasi-steady-state approximation is further employed to study the linear stability analysis with time-varying state variables by numerical simulations (Skarbek et al., 2012; Luo and Ampuero, 2018). The results show that the approximate solution for the system's critical stiffness is consistent with the numerical solution (Fig. 3(a)), indicating that the simplification of the system is reasonable.

2.4 Applicability boundaries of the quasi-steady-state approximation

A rigorous analysis of the validity of the quasi-steady-state approximation (QSSA) employed in the linear stability analysis is carried out. The QSSA assumes that the pore pressure field evolves sufficiently slowly that it can be considered constant, while the frictional state variables of the system undergo rapid changes towards equilibrium. Following the singular perturbation framework established by Segel and Slemrod (1989), the parameters governing the accuracy of this approximation are identified and its applicability boundaries are quantified.

2.4.1 Timescale identification

The core of singular perturbation analysis is the separation of timescales and the identification of characteristic timescales for the fast and slow processes.

Frictional state (fast) timescale (χ_θ). In the absence of the effective normal stress term, the characteristic timescale for the process of the state variable evolution is the time it takes to slip a distance d_c at a reference velocity. Accordingly, the frictional state timescale χ_θ is defined as:

$$\chi_\theta = \frac{d_c}{v_0} \tag{29}$$

This is the timescale for the state variable to relax towards its steady-state value for a fixed pore pressure and normal stress.

Pore pressure (slow) timescale (χ_p). The characteristic timescale χ_p of pore pressure evolution is determined by the coefficient in the relaxation term:

$$\chi_p = \frac{1}{c} = \frac{\eta L V_0 \beta}{\kappa A} \tag{30}$$

This represents the time it takes for the pore pressure to equilibrate with the ambient pressure p_0 due to diffusion.

2.4.2 Dimensionless formulation and perturbation parameter

In order to make the equations dimensionless, time is scaled by the fast timescale. Let $\chi = t/\chi_\theta$ be the dimensionless time, then the governing Eqs. (2) and (4) become:

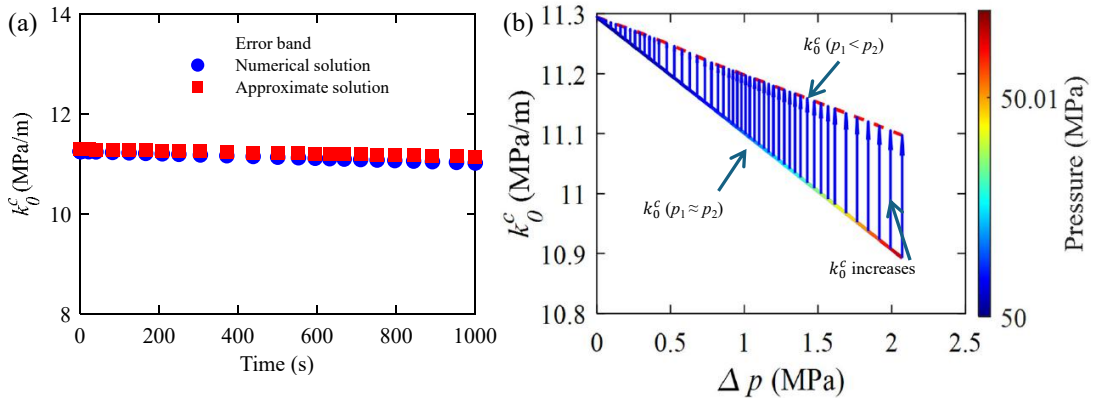

Fig. 3. (a) Comparison of the approximate solution (Eq. (28)) and numerical solution, and (b) the fluid pressure distribution Δp ($\Delta p = p_2 - p_1$) as a function of the critical stiffness. $q_2 = 0.001$ kg/s, $c = 0.00001$, $N = 2$.

$$\frac{\partial \theta_i}{\partial \chi} = -\frac{v_i}{v_0}\left(\theta_i + b\ln\frac{v_i}{v^*}\right) - \frac{\chi_\theta}{\sigma_i'}\frac{\partial \sigma_i'}{\partial \chi} \tag{31}$$

$$\frac{\partial p_2}{\partial \chi} = \frac{\chi_\theta}{\chi_p}(p_0 - p_2) + \chi_\theta l q_2 \tag{32}$$

The key dimensionless group that emerges is the ratio of the fast to the slow timescale, ε:

$$\varepsilon = \frac{\chi_\theta}{\chi_p} = c\chi_\theta = \frac{c d_c}{v_0}, \tag{33}$$

which is the singular perturbation parameter. The QSSA is mathematically justified when $\varepsilon < 1$. Given this limit, Eq. (32) becomes:

$$\frac{\partial p_2}{\partial \chi} = \varepsilon(p_0 - p_2) + \chi_\theta l q_2 \tag{34}$$

This implies that the dimensionless rate of pressure change $\partial p_2/\partial \chi$ is of order ε, confirming that pressure is indeed a slow variable evolving on a timescale $\chi_p = \chi_\theta/\varepsilon > \chi_\theta$.

2.4.3 Validity conditions for QSSA

For the QSSA to be valid, two primary conditions must be met:

Timescale separation condition. The pore pressure must evolve much more slowly than the state variable, which requires the perturbation parameter to be small:

$$\varepsilon = \frac{c d_c}{v_0} < 1 \tag{35}$$

Small injection perturbation condition. Even if ε is small, a very high injection rate q_2 could cause a rapid pressure change during the fast frictional adjustment time χ_θ, violating the assumption of a quasi-static pressure field. The pressure change due to injection during the time χ_θ must be small compared with a reference pressure (p_0):

$$|\Delta p| \approx |\dot{p}_2|\chi_\theta = |l q_2|\chi_\theta = \frac{l q_2 d_c}{v_0} < p_0 \tag{36}$$

This leads to the second dimensionless parameter:

$$\varsigma = \frac{l q_2 d_c}{v_0 p_0} < 1 \tag{37}$$

Here, a threshold of 0.1 is chosen, i.e., $\varepsilon \le 0.1$ and $\varsigma \le 0.1$, implying that the time scale of the slow process is at least ten times that of the fast process. Under this condition, the criterion is converted into constraints on the model parameters c and lq_2. The results show that the applicability boundaries of the QSSA during dynamic diffusion processes are $0 \le c \le 0.001$ and $0 \le lq_2 \le 0.03$.

2.5 Influence of pressure heterogeneity on local chemical reaction rates

Here, the temperature T is assumed to remain approximately constant in time and space (taken as the reference temperature T_0) during the second-level dynamic process, and the feedback of the mass-thermal coupling is neglected.

The pressure-sensitive form of the reaction rate $\mathscr{W}_p(p,T)$ is obtained from the transition state theory (TST) (Eyring, 1935):

$$\mathscr{W}_p(p,T) \propto \exp\left(-\frac{\Delta G^\ddagger(p,T)}{RT}\right) \tag{38}$$

where $\Delta G^\ddagger$ represents the activated free energy, $\mathscr{W}_p$ represents the reaction rate, p represents the pore pressure, R is the universal gas constant, and T represents the Kelvin temperature. The activation volume $\Delta V^\ddagger$ is defined as:

$$\Delta V^\ddagger = \left(\frac{\partial \Delta G^\ddagger}{\partial p}\right)_T \tag{39}$$

Linearizing $\Delta G^\ddagger$ at fixed T gives:

$$\Delta G^\ddagger(p,T) = \Delta G^\ddagger(p_0,T) + \Delta V^\ddagger(p - p_0) + \cdots \tag{40}$$

Taking the first order and absorbing the constant term into the prefactor $\mathscr{W}_{p_0}(T)$ obtains:

$$\mathscr{W}_p(p,T) = \mathscr{W}_{p_0}(T)\exp\left(-\frac{\Delta V^\ddagger p}{RT}\right) \tag{41}$$

The prefactor $\mathscr{W}_{p_0}(T)$ can be written in the form of Arrhenius $\mathscr{W}_0(T) = W\exp(-E_a/RT)$, thus:

$$\mathscr{W}_p(p,T) = W\exp\left(-\frac{E_a}{RT}\right)\exp\left(-\frac{\Delta V^\ddagger p}{RT}\right) \tag{42}$$

where W is a pre-exponential factor and E_a represents the activation energy. Taking the logarithm of the above expression and fixing it at T:

$$\left(\frac{\partial \ln \mathscr{W}_p}{\partial p}\right)_T = -\frac{\Delta V^{\ddagger}}{RT} \tag{43}$$

Let:

$$S_p = \frac{|\Delta V^{\ddagger}|}{RT_0} \tag{44}$$

where S_p is a dimensionless pressure-sensitivity parameter. If $\Delta V^{\ddagger} < 0$, an increase in pressure causes $\mathscr{W}_p$ to increase exponentially.

When $p = p_0 + \tilde{p}$ at $T = T_0$ (approximate at room temperature), then:

$$\frac{\mathscr{W}_p(p, T_0)}{\mathscr{W}_p(p_0, T_0)} = \exp\left(-\frac{\Delta V^{\ddagger}\tilde{p}}{RT}\right) = \exp(S_p\tilde{p}) \quad (\text{if } \Delta V^{\ddagger} < 0) \tag{45}$$

where $\tilde{p}$ denotes the pressure fluctuation around the reference pressure p_0. For zero-mean pressure fluctuations, $\langle\tilde{p}\rangle = 0$ with the variance $\langle\tilde{p}^2\rangle$, where $\langle\cdot\rangle$ represents a spatial (or ensemble) average. The exponential function is convex, therefore:

$$\frac{\langle\mathscr{W}_p\rangle}{\mathscr{W}_p(p_0, T_0)} = \langle\exp(S_p\tilde{p})\rangle \geq \exp(S_p\langle\tilde{p}\rangle) = 1 \tag{46}$$

If the disturbance is small, the second-order Taylor expansion is used:

$$\frac{\langle\mathscr{W}_p\rangle}{\mathscr{W}_p(p_0, T_0)} \approx 1 + \frac{1}{2}S_p^2\langle\tilde{p}^2\rangle \geq 1 \tag{47}$$

Even if the average pressure disturbance in space is zero, the heterogeneity of pressure distribution will inevitably lead to a higher average reaction rate than that under a uniform pressure field. Moreover, the relative increase in the average reaction rate is approximately equal to half of the product of the square of the pressure sensitivity and the variance of the pressure fluctuation. For a finite pressure difference Δp, where Δp is the characteristic amplitude of the pressure variation, Eq. (42) gives:

$$\mathscr{W}_p(p_0 + \Delta p) = \frac{\mathscr{W}_p(p_0 + \Delta p, T_0)}{\mathscr{W}_p(p_0, T_0)} = \exp\left(\frac{|\Delta V^{\ddagger}|}{RT_0}\Delta p\right) \tag{48}$$

3. Results

3.1 Pressure distribution and fault stability

The influence of fluid pressure distribution on fault stability is first examined by analyzing the evolution of critical stiffness during fluid injection and its dependence on pressure heterogeneity along the fault. Fig. 3 depicts the evolution of critical stiffness (k_0^c) with fluid injection time (Fig. 3(a)) and the relationship between k_0^c and pressure difference Δp (Fig. 3(b)); p_1 and p_2 in Fig. 3(b) represent the fluid pressure at the diffusion point (slider 1) along the fault and at the injection point (slider 2), respectively, with Δp ($\Delta p = p_2 - p_1$, Eq. (6)) denoting the pressure difference between these two points. Hereinafter, Δp is used to describe the fluid pressure distribution along the fault. $\Delta p \approx 0$ represents a homogeneous fluid pressure distribution, while a positive value of Δp (> 0) indicates a heterogeneous pressure distribution. In the case of homogeneous fluid pressure (marked by a colored line in Fig. 3(b), not to the X-axial scale), the increase in fluid pressure results in a decrease in k_0^c. In the case of heterogeneous fluid pressure ($\Delta p > 0$), an increase in Δp results in a reduction of the critical stiffness k_0^c (red dashed line in Fig. 3(b)). The blue arrows in Fig. 3(b) indicate the relative change in critical stiffness when the heterogeneity of fluid pressure is considered. As Δp increases, the magnitude of the increase in critical stiffness also grows. This indicates that fluid pressure heterogeneity increases the critical stiffness threshold required for fault stability, counteracting the stable effect of high fluid pressure (the blue arrows in Fig. 3(b)). In qualitative terms, this is consistent with the results in the experiment, where fluid injection into faults leads to stress heterogeneity, causing fault instability (Cebry and McLaskey, 2021).

3.2 Injection-diffusion controls on fault stability

To further understand how the heterogeneity of fluid pressure promotes instability in earthquake faults, different scenarios with varying parameters q and c were simulated, and the resulting pressure distribution profile, the moment magnitude, the number of dynamic events (Fig. 4(a)), the critical stiffness of the system (Fig. 4(b)) and potential for earthquake fault instability (Fig. 4(c)) were evaluated. As shown in Fig. 4(a), when other parameters are constant, a higher injection rate (Hereinafter, q specifically refers to the injection rate q_2. $q = 0.001$ kg/s) leads to a more pronounced heterogeneity in the pressure profile (the pressure $p_{2,q}$ at injection is greater than the pressure $p_{1,q}$ at diffusion) along the fault (the green squares in Fig. 4(a)), a higher critical stiffness (Fig. 4(b)), a higher moment magnitude (M_w-2.98), and more dynamic events (Y=3). This indicates that the fluid pressure heterogeneity generated by a high injection rate increases the risk of earthquakes. In the case of a lower diffusion coefficient (c=0.000001), a result similar to that for a higher injection rate is obtained. The low c may result in a stronger heterogeneity in pressure profile along the fault (the magenta triangles in Fig. 4(a)), a higher critical stiffness (Fig. 4(b)), a higher moment magnitude (M_w -2.83) and more dynamic events ($Y = 4$). All these results from the simulation of this study are consistent with previous experimental observations. For instance, the experiment conducted on shale fault gouge (Scuderi and Collettini, 2018) and PMMA (Cebry and McLaskey, 2021) showed that the heterogeneous diffusion of fluid results in the accelerated and unstable sliding of faults. Fig. 4(c) also shows, for different injection rates q, how the normalized pressure heterogeneity required for the first rupture varies with the diffusion coefficient c. Here, the pressure heterogeneity is defined as p_2/p_1, and its normalized form is given by $f = [p_2/p_1 - \min(p_2/p_1)] / [\max(p_2/p_1) - \min(p_2/p_1)]$. As c decreases, the system exhibits higher pressure heterogeneity and earlier onset of slip. Likewise, when c is kept fixed, increasing q enhances the heterogeneity and advances rupture initiation. These results indicate that systems with low diffusivity and high injection rates develop local pressure heterogeneity earlier and more readily, resulting in greater system instability.

Since the effects of q and c on fault stability are mediated

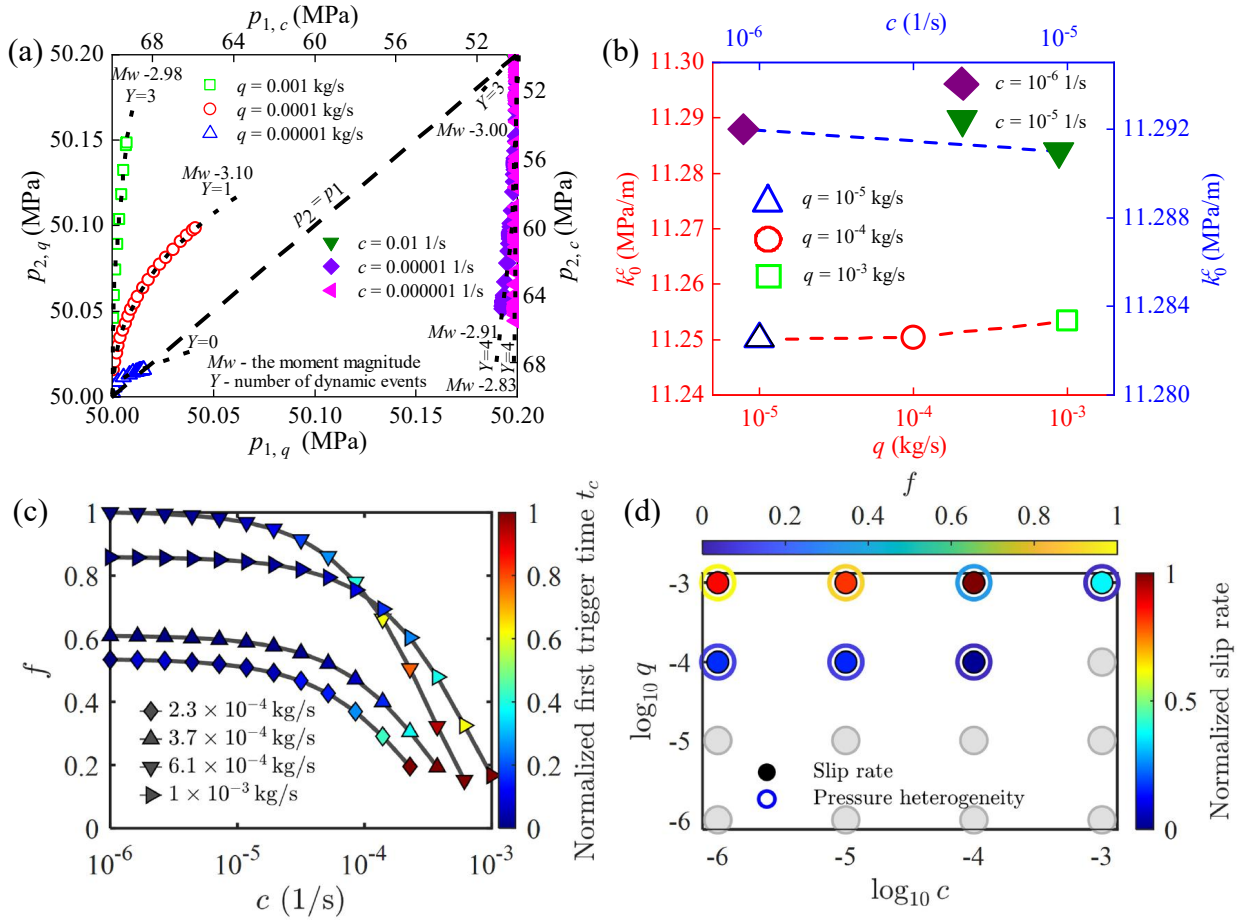

Fig. 4. (a) Fluid pressure distribution, (b) maximum critical stiffness of the system corresponding to each case in (a), (c) effect of diffusion coefficient on normalized pressure heterogeneity and (d) phase diagram of earthquakes.

by the fluid-pressure heterogeneity, it is important to examine how this heterogeneity relates directly to slip velocity and seismicity. In Fig. 4(d), the relationship between the maximum slip velocity of faults and fluid pressure heterogeneity is shown. Each solid circle in Fig. 4(d) represents the maximum slip velocity, and each hollow circle indicates fluid pressure heterogeneity with a particular injection rate q and a particular diffusivity c. The colored points mark the occurrence of earthquakes (i.e., stick-slip events), and the gray color represents the absence of earthquakes in Fig. 4(d). A low diffusion coefficient and a high injection rate are found to increase the maximum slip velocity of the fault. Notably, the heterogeneity of fluid pressure distribution shows a strong consistency with the occurrence of earthquakes, which implies that pressure heterogeneity may play an important role in controlling fault instability.

3.3 Influence of pressure heterogeneity magnitude on fault slip

Pressure heterogeneity is a key factor controlling the transition from aseismic to seismic slip. By systematically varying its magnitude, we can examine how changes in heterogeneity affect fault stability. The results presented in Fig. 5 illustrate the influence of the magnitude of pressure heterogeneity on fault stability. Fig. 5(a) demonstrates a clear transition in fault behavior from aseismic to seismic as the pressure heterogeneity magnitude increases (the dashed red line). For low heterogeneity magnitude (< 0.1), the system predominantly exhibits stable creep, with maximum slip velocities (v_m) remaining below the seismic slip threshold (the dashed black line). In contrast, for a high heterogeneity magnitude, fault slip becomes increasingly unstable, characterized by rapid acceleration. This transition suggests that higher pressure heterogeneity magnitude facilitates seismic slip. Fig. 5(b) shows the temporal evolution of slip for different pressure heterogeneity magnitudes. The results indicate that under low heterogeneity magnitude, slip accumulates gradually, consistent with the stable sliding behavior. However, as heterogeneity increases, the slip evolution exhibits stick-slip frictional behavior, i.e., the mechanism for seismic slip, indicative of dynamic rupture events. This transition corresponds to the regime shift observed in the Fig. 5(a), reinforcing the hypothesis that pressure heterogeneity plays a critical role in controlling fault stability.

4. Discussion

This study presents a new nucleation model based on the classical RSF, which indicates that the frictional instability of the spring-slider system depends not only on the injection fluid

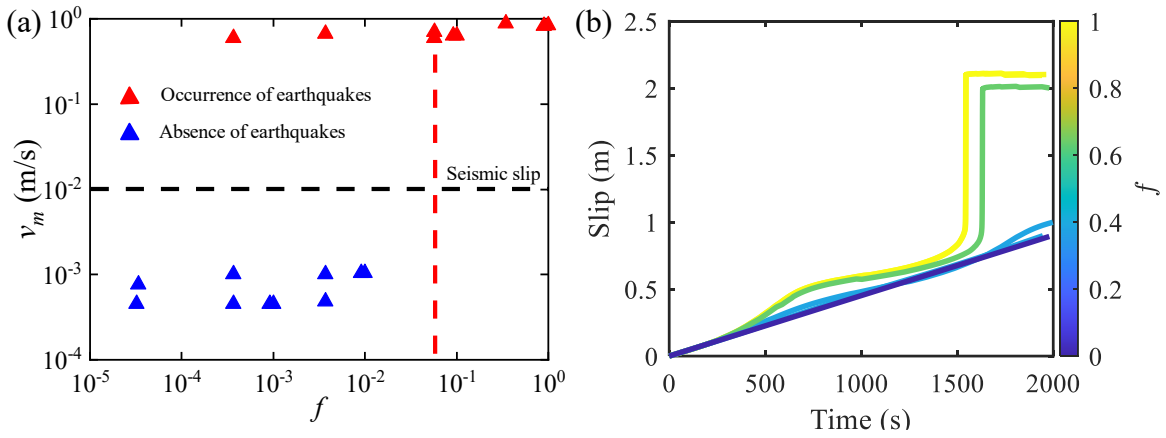

Fig. 5. (a) Maximum slip velocity of faults under different pressure heterogeneity magnitudes and (b) temporal evolution of slip for different pressure heterogeneity magnitudes.

Table 2. Summary of the characteristics of different models and the main influencing factors.

Models	Model features	Main factors
The model in this study	Incorporates fluid injection and diffusion	Fluid pressure distribution
Ruina (1983)	Introduces pore pressure	Normal stress, pore pressure
Linker and Dieterich (1992)	Considers the effect of variable normal stress	Variable normal stress
Alghannam and Juanes (2020)	Emphasizes the competitive effect between fluid pressure and its rate of change	Pore pressure, rate of pore pressure change, hydraulic diffusivity
Sun et al. (2024)	Incorporates changes in inertial effects	Effective normal stress and radiation damping

Notes: Only representative models and characteristics related to the fluid pressure are summarized here.

pressure but also on the diffusing pressure along the fault. As the fluid pressure evolves from the initial state to a steady state due to fluid injection and diffusion, the distribution of fluid pressure along the fault plays a crucial role in controlling fault stability.

The findings of this study enhance previous RSF-based nucleation models thanks to incorporating the process of fluid diffusion along the fault and integrating it with the fluid injection process. The proposed nucleation model suggests that high fluid pressure makes a fault stable, whereas the heterogeneous pressure distribution along the fault counteracts this stable effect. Furthermore, the stability of seismic faults is affected by the injection rate of fluid and the diffusion coefficient of faults. As the injection rate increases or the diffusion coefficient decreases, the fluid does not diffuse fast enough and might be forced to flow along narrow channels, thus promoting pressure heterogeneity (Shvarts and Yastrebov, 2018). Importantly, a higher pressure heterogeneity magnitude may lead to greater fault instability and an increased likelihood of seismic slip.

4.1 Comparison with classical nucleation models

The similarities and differences among various earthquake nucleation models are summarized in Table 2. The model of this study indicates that the critical stiffness of the loading system is governed by two parts: Fluid injection ($i = 2$) and diffusion along faults ($i = 1$), and it is influenced by parameters such as injection rate q, pore pressure p_i, diffusion coefficient c, and so on. When fluid diffusion along the strike is not considered, the critical stiffness of the loading system in this study becomes $k_0^c = (b-a)(\sigma - p_2)/d_c + \alpha/v_0\dot{p}_2$. The total system stiffness degrades to the critical stiffness form of a single slider, as defined by Alghannam and Juanes (2020). When the injected fluid is not considered, the critical stiffness of the loading system further becomes $k_0^c = (b-a)(\sigma - p_2)/d_c$, and the total system stiffness degrades to the critical stiffness form as defined by Ruina (1983). Sun et al. (2024) focused on how the interaction between the rate of change of effective stress and inertial effects influences fault-slip behavior, demonstrating this behavior at the critical stiffness $k_0^c = -\alpha(\dot{\sigma} - \dot{p})/v_0 + (b-a)(\sigma - p)/d_c + \zeta\,[(\dot{\sigma} - \dot{p})/(\sigma - p) - v_0/d_c]$, where ζ represents the radiation-damping approximation. The rate of change in effective stress is a key factor determining whether fault slip will be aseismic (slow, gradual movement) or seismic (rapid, earthquake-generating slip), especially when injection rates change suddenly. Inertial effects, on the other hand, tend to suppress the transition to seismic slip during injection.

4.2 Pressure-heterogeneity threshold universality

The pressure heterogeneity f quantifies the intensity of local pressure differences (gradients) within the pressure field. When f exceeds a certain threshold f_c, it can induce slip

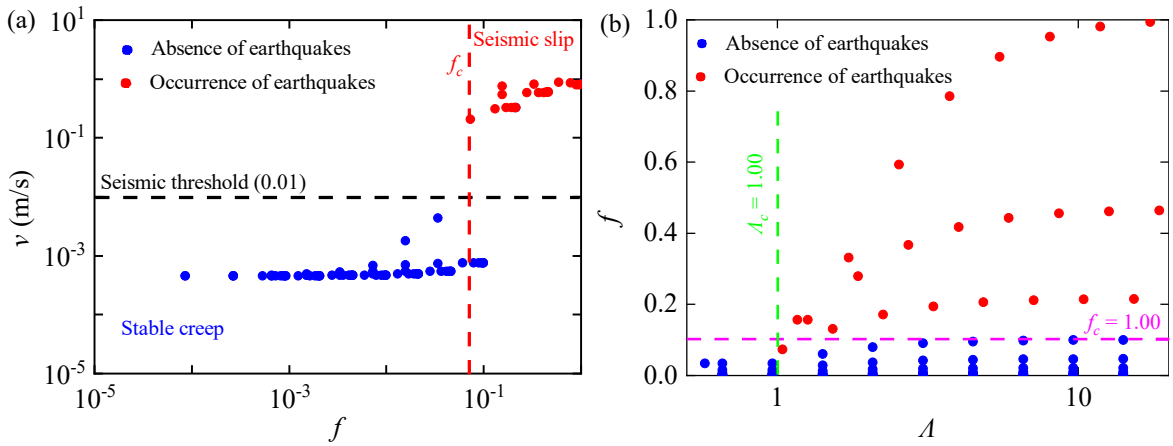

Fig. 6. (a) Slip velocity of faults under different pressure heterogeneity magnitudes and (b) pressure heterogeneity magnitudes under different characteristic diffusion lengths.

instability. The threshold f_c represents the minimum degree of heterogeneity in fluid pressure perturbations required to trigger rupture (Fig. 5(a)). Here, multiple parameter combinations are examined again. The results show that this heterogeneity threshold remains stable across a wide range of parameter variations, with a value of approximately 0.1 (Fig. 6(a)). From the previous analysis, the diffusion coefficient $c = \kappa A/\eta L V_0 \beta$ is obtained. Accordingly, the characteristic diffusion length L is given by:

$$L = \frac{\kappa A}{\eta c V_0 \beta} \tag{49}$$

The characteristic diffusion length is related to the permeability κ of rocks, the viscosity η of fluids, compressibility β, and so on. The critical timescale t_c is defined as the time required to reach the seismic velocity. Meanwhile, a dimensionless diffusion length Λ is introduced:

$$\Lambda = \frac{L}{\sqrt{D t_c}} \tag{50}$$

where D represents the comprehensive hydraulic diffusion coefficient. The pressure equation is then reformulated into the standard diffusion equation form:

$$\frac{\partial p}{\partial t} = D \nabla^2 p \tag{51}$$

By performing dimensional analysis, the following expression is obtained:

$$[c] = \frac{1}{t} \rightarrow D \propto \frac{L^2}{c^{-1}} = L^2 c \tag{52}$$

Then, the comprehensive hydraulic diffusion coefficient D can be defined as:

$$D = \xi L^2 c \tag{53}$$

where ξ is a dimensionless geometric factor. In this study, for one dimensional diffusion, ξ takes the value of 1. Substituting D into Λ yields:

$$\Lambda = \frac{1}{\sqrt{c t_c}} \tag{54}$$

This dimensionless diffusion length Λ unifies the scale of the coupled diffusion-slip processes under different parameters. As shown in Fig. 6(b), for different values of Λ, the heterogeneity f is always below a threshold, and below this threshold, the slip velocity is all less than 0.01 m/s. This indicates that even when the diffusion distance is small, insufficient pressure heterogeneity will not trigger unstable slip (blue markers). Only when f exceeds a certain threshold does the system trigger seismic slip, regardless of the value of Λ. The results suggest that this threshold reflects a universal instability criterion inherent to the system, rather than an incidental product of a specific fault or rock type. In this way, the heterogeneity threshold exhibits both parameter invariance and dynamical universality, supporting its role as a general controlling factor for rupture initiation.

4.3 Three-slider validation in pressure-heterogeneity threshold

Compared with continuum models, the spring-slider system simplifies the pressure distribution along the fault. To evaluate the potential influence of spatial pressure gradients that may be neglected under this simplification, a three-degrees-of-freedom spring-slider model is investigated. This system incorporates the second-order spatial effects that are lacking in the two-slider system. While keeping all model parameters fixed, additional simulations of the three-slider system are performed. In this simulation, as in the two-slider case, fluid is injected at the rightmost slider and diffuse toward the left (Fig. 7(a)). The results show a clear pressure heterogeneity threshold in the three-spring-slider system (dashed green line in Fig. 7(b)), above which fault instability is triggered. The threshold given from the three-spring-slider model is slightly higher than that of the two-slider system (dashed red line in Fig. 7(b)), with a difference of approximately 0.003. Such a minor difference indicates that the conclusions drawn from the two-slider model are robust. These results suggest that the threshold for fault instability is mainly governed by the existence of pressure heterogeneity, whereas the detailed spatial distribution of pressure gradients (e.g., linear versus nonlinear

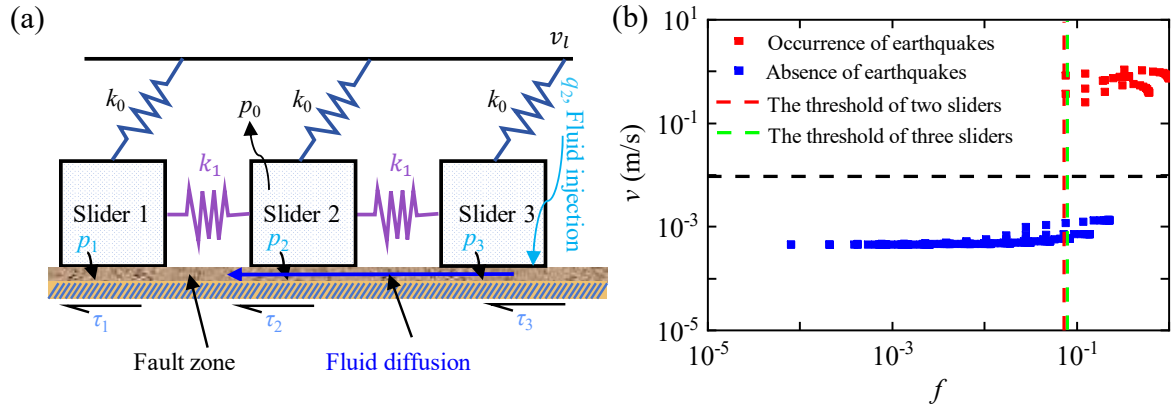

Fig. 7. (a) The three-degrees-of-freedom spring-slider model and (b) pressure heterogeneity thresholds in two- and three-degrees-of-freedom spring-slider models.

variations between sliders) exerts only a little influence on the instability threshold. This indicates that, although the two-degree-of-freedom spring-slider system does not explicitly describe the continuous gradient between fault segments, it can already capture the first-order effects of spatial pressure gradients on the instability threshold. Continuum models are expected to yield consistent results but may provide more detailed information on the rupture dynamics, which will be the focus of future work.

4.4 Predictions of model results

This study explores a model ($N = 2$) to describe the sliding behavior of seismic faults and fluid pressure change, considering an injection well where fluid is injected and a monitoring well where fluid is passed through. In this model, slider-2 represents the injection point and slider-1 represents the monitoring well. The results show that the pressure at the monitoring well shows only a tiny increase under constant permeability throughout the time window (dashed black line in Fig. 8(a)). In comparison to the observations from the one dimensional diffusion model and laboratory experiments (Cebry and McLaskey, 2021), the changes in fluid pressure in the early stage of injection are quite similar in these three cases, but in the later stage, the fluid pressure increases rapidly in the experimental results (solid blue line in Fig. 8(a)). This difference is attributed to the high compliance of PMMA used in the experiments. The fault is likely to produce fault-normal displacements during injection (Cappa et al., 2022), which opens up pathways for fluid migration and pressure diffusion (Witherspoon et al., 1980). The influence of PMMA compliance on the diffusion process can be quantitatively captured through a pressure-dependent permeability relationship. The dilation effect of PMMA induces dynamic changes in permeability. Specifically, permeability κ increases with elevated fluid pressure p, and its evolution can be described by the equation $\kappa = \kappa_{\min} + (\kappa^* - \kappa_{\min})e^{-(\sigma - p)/\sigma^*}$ (Cruz-Atienza et al., 2018; Zhu et al., 2020), where κ^* is a reference permeability, and it satisfies $\partial\kappa^*/\partial t = -v/L(\kappa^* - \kappa_{\max})$; σ^* is a stress-sensitivity parameter determined by experiments, $\kappa_{\min}$ is a minimum bound on permeability, with a value of 10^{-15} m^2, and $\kappa_{\max}$ is a maximum bound on permeability, equal to 10^{-12} m^2. Incorporating this pressure-dependent permeability into the model in this study yields a pressure evolution line (dashed red line in Fig. 8(a)) that aligns more closely with the PMMA experimental observations (solid blue line in Fig. 8(a)). Due to the simplicity of the model, more realistic fault conditions, such as complex fault geometries, cannot be represented, prompting further investigations in the future.

Additionally, experimental data from Passelègue et al. (2020) and Cebry and McLaskey (2021) are incorporated into the analysis. The results indicate that the heterogeneity of fluid pressure along the fault increases the number of dynamic events and the moment magnitude (M_w), promoting fault instability (Fig. 8(b)). A further analysis of the fluid pressure along the fault (at both the injection and monitoring locations) is conducted for these experiments (Fig. 8(c)). The results show that once the pressure heterogeneity exceeds a certain threshold (approximately 0.1), fault slip transitions from stable creep to unstable acceleration (Fig. 8(d)). This behavior is consistent with the predictions of the model in this study (dashed red line in Fig. 8(d)), indicating that strong fluid pressure heterogeneity can significantly enhance fault slip activity. This alignment highlights the relevance of these findings and strengthens the evidence for the proposed mechanism.

4.5 Effects of pressure heterogeneity on local chemical reaction rates

The pressure heterogeneity may locally accelerate exothermic reactions like serpentinization by reducing the activation barrier. The rate constant scales as $\mathscr{W}_p \propto \exp(-\Delta V^{\ddagger} p/RT)$, where a negative activation volume ($\Delta V^{\ddagger} < 0$) means that positive pressure excursions exponentially enhance local rates; $\mathscr{W}_p$ represents the reaction rate; R is the gas constant; T denotes the Kelvin temperature. Crucially, the convexity of this function implies that spatial variations elevate the mean reaction rate $\langle \mathscr{W}_p \rangle$ above the homogeneous case $\mathscr{W}_p(p_0)$ via $\langle \mathscr{W}_p \rangle / \langle \mathscr{W}_p(p_0) \rangle \geq 1 + (|\Delta V^{\ddagger}|/RT_0)^2 \langle \tilde{p}^2 \rangle$, where T_0 is an approximation at room temperature. Order-of-magnitude esti-

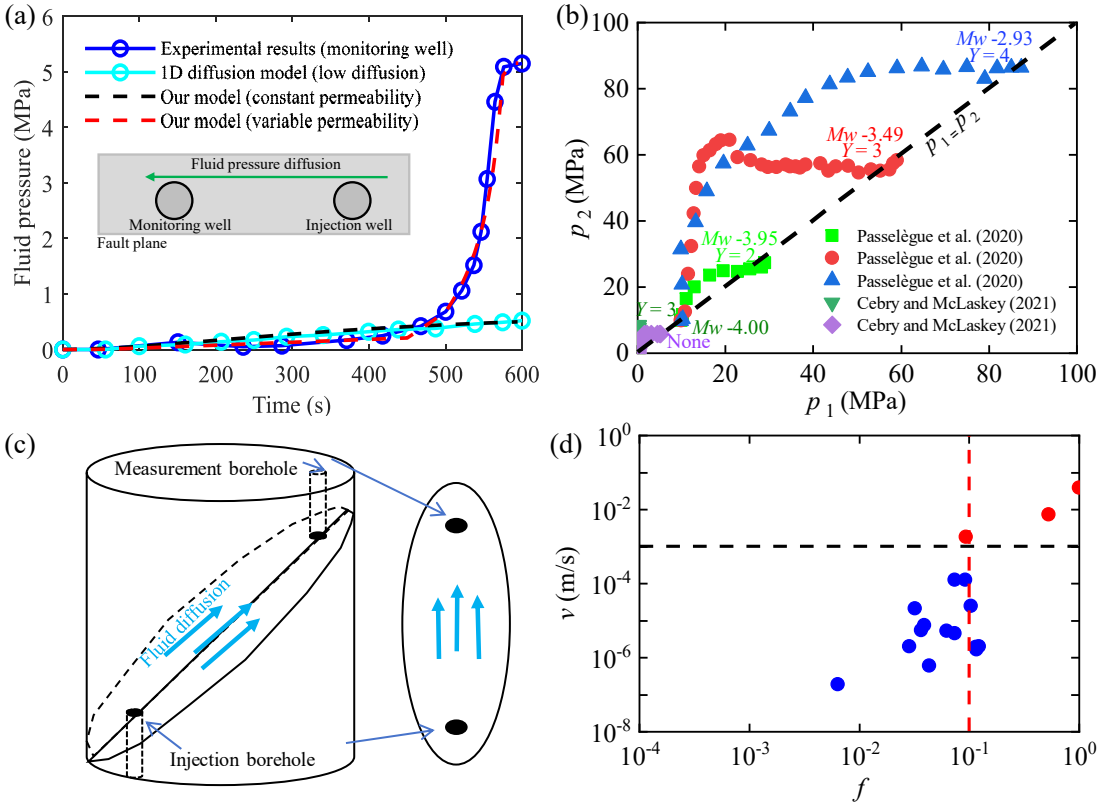

Fig. 8. (a) Measured pressures in monitoring wells for different models, (b) fluid-pressure profiles along faults, (c) schematic of the sample assembly and (d) fault slip velocity for different pressure heterogeneities. After Passelègue et al. (2020) and Cebry and McLaskey (2021).

mates using realistic parameters ($\Delta V^{\ddagger} \approx -5 \times 10^{-6}$ m^{3}mol^{-1}, $\tilde{p} \approx 50$ MPa) suggest that local rate enhancements can exceed 7%. These findings identify pressure heterogeneity as a potential driver for creating reaction hotspots independent of longer-term thermo-chemical feedbacks.

4.6 Implications of fault geometry for fault stability

This study employs a simplified one-dimensional fault model to highlight the fundamental role of spatially heterogeneous fluid pressure in controlling fault stability. However, it should be noted that fault geometry, including dip angle, segmentation, and branching structures, plays a critical role in governing rupture behavior. Geometric irregularities can alter the orientation of the stress field and pathways of fluid migration, thereby generating local variations in effective stress along the fault that may either enhance or counteract the stabilizing effect of high fluid pressure. Previous studies have demonstrated that the geometric structure of fault networks significantly affects strain localization, rupture propagation, and fluid-stress interactions, thereby determining whether a fault segment undergoes stable slip or dynamic rupture (Ross et al., 2020; Hui et al., 2023; Lee et al., 2024; Roche et al., 2025). Faults with more complex geometries tend to exhibit stronger stress and strength heterogeneities, making them more susceptible to local instabilities or multi-segment cascading ruptures under non-uniform pore-pressure conditions. The present model is limited by its one-dimensional fault representation, which neglects the complex geometric effects of fault dip, segmentation, and branching. Therefore, future studies should incorporate realistic fault geometries into multi-dimensional coupled hydro-mechanical models to achieve a deeper understanding of how fault structure regulates fluid-induced fault instability.

4.7 Pressure-heterogeneity index for an early warning system

To operationalize the heterogeneity-centric mechanism, a dimensionless pressure-heterogeneity index f is proposed as a real-time precursor. The model in this study demonstrates that when f approaches and exceeds ~ 0.1, the probability of transition from stable creep to unstable stick-slip increases sharply, and this threshold is robust and universal across a wide parameter ranges. Accordingly, the index f is embedded in a traffic-light protocol: Low values permit routine operation, intermediate values trigger intensified monitoring and moderate rate reduction, and high values prompt temporary shut-in/bleed-off and risk reassessment. The workflow centers on the online estimation of $p(x,t)$ and f on a fault plane (or monitoring profile) from wellhead/downhole pressure, DAS/DTS, GNSS/InSAR and microseismic data, with site-specific calibration of the threshold using retrospective records

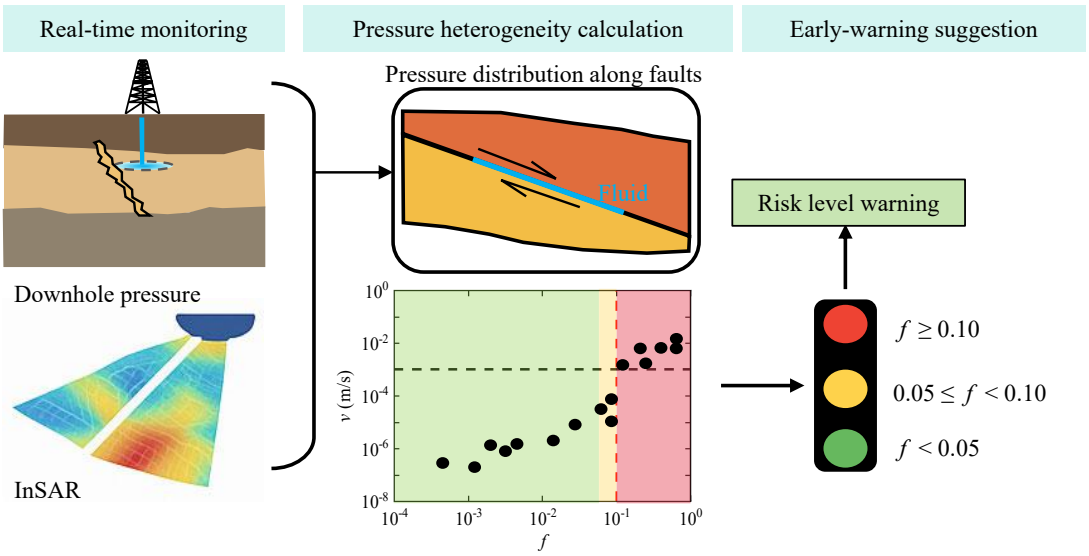

Fig. 9. Monitoring of stress heterogeneity and traffic light protocols.

– thereby turning a theoretical criterion into an actionable engineering rule (Fig. 9).

5. Conclusions

This study provides a new perspective to understand the role of fluids in earthquake nucleation and offers a potential explanation for the debate on whether high fluid pressure stabilizes or destabilizes faults with regard to the results of the field, laboratory experiments and the RSF model. The main conclusions can be summarized as follows:

1) A new two-degree-of-freedom spring-slider model is developed, that is based on the classical rate-and-state friction (RSF) framework and incorporates fluid injection and diffusion, and the stability criterion of the system is extended. This criterion indicates that high fluid pressure tends to stabilize faults, whereas along-fault fluid pressure heterogeneity counteracts this stabilizing effect.
2) Increasing the injection rate or reducing the diffusion coefficient enhances pressure heterogeneity. The along-fault heterogeneity of fluid pressure closely coincides with the occurrence of earthquakes, implying that pressure heterogeneity is a likely driver of fault instability.
3) The magnitude of high pressure heterogeneity may lead to greater instability in faults and an increased likelihood of seismic slip. As pressure heterogeneity increases, the evolution of fault slip exhibits a transient from stable creep to unstable stick-slip. This corresponds to a pressure-heterogeneity threshold that remains robust across wide parameter variations, at approximately 0.1. This threshold reflects a universal instability criterion inherent to the system, rather than an incidental product of a specific fault or rock type, and its parameter invariance and dynamical universality support its role as a universal controlling factor for fault rupture occurrence.

By monitoring the pressure heterogeneity of the fault, it is possible to predict whether it may enter an unstable slip state. The monitoring of pressure-heterogeneity index is proposed as an operational precursor to unstable slip. Elevated heterogeneity should trigger heightened observation and, where applicable, the adaptive control of injection rates in traffic-light-style protocols. Furthermore, to extrapolate this model to a wide range of scenarios in the field, the distribution of pore fluid pressure may provide a new insight into fluid-induced earthquakes and seismic swarms along the subduction zone.

To broaden the applicability of the proposed model, future work should embed this heterogeneity mechanism within complex fault geometries (branching, roughness, multifault networks) and continuous poroelastic media with anisotropic and evolving permeability, and explore thermo-hydro-mechanical coupling and frictional complexity. Coupling the model with dense pressure measurements and microseismic imaging via data assimilation and uncertainty quantification will enable prospective tests of heterogeneity-based forecasting in both induced and natural seismicity, including subduction-zone swarms.

Acknowledgements

This work was funded by the fellowship from the Horizon2020 BESTOFRAC (No. 734370). Shao-bo Han acknowledges the financial support from the China Scholarship Council (No. 202106440016).

Conflict of interest

The authors declare no competing interest.

References

Abe, Y., Kato, N. Complex earthquake cycle simulations using a two-degree-of-freedom spring-block model with a rate-

and state-friction law. Pure and Applied Geophysics, 2013, 170(5): 745-765.

Alghannam, M., Juanes, R. Understanding rate effects in injection-induced earthquakes. Nature Communications, 2020, 11(1): 3053.

Anyim, K., Gan, Q. Fault zone exploitation in geothermal reservoirs: Production optimization, permeability evolution and induced seismicity. Advances in Geo-Energy Research, 2020, 4(1): 1-12.

Atkinson, G. M., Eaton, D. W., Igonin, N. Developments in understanding seismicity triggered by hydraulic fracturing. Nature Reviews Earth & Environment, 2020, 1(5): 264-277.

Bedford, J. D., Faulkner, D. R., Allen, M. J., et al. The stabilizing effect of high pore-fluid pressure along subduction megathrust faults: Evidence from friction experiments on accretionary sediments from the Nankai Trough. Earth and Planetary Science Letters, 2021, 574: 117161.

Biot, M. A. General theory of three-dimensional consolidation. Journal of Applied Physics, 1941, 12(2): 155-164.

Bos, B., Spiers, C. J. Fluid-assisted healing processes in gouge-bearing faults: Insights from experiments on a rock analogue system. Pure and Applied Geophysics, 2002, 159(11): 2537-2566.

Burridge, R., Knopoff, L. Model and theoretical seismicity. Bulletin of the Seismological Society of America, 1967, 57(3): 341-371.

Byerlee, J. The mechanics of stick-slip. Tectonophysics, 1970, 9(5): 475-486.

Cappa, F., Guglielmi, Y., Nussbaum, C., et al. Fluid migration in low-permeability faults driven by decoupling of fault slip and opening. Nature Geoscience, 2022, 15(9): 747-751.

Cappa, F., Scuderi, M. M., Collettini, C., et al. Stabilization of fault slip by fluid injection in the laboratory and *in situ*. Science Advances, 2019, 5(3): eaau4065.

Cebry, S. B. L., McLaskey, G. C. Seismic swarms produced by rapid fluid injection into a low-permeability laboratory fault. Earth and Planetary Science Letters, 2021, 557: 116726.

Cruz-Atienza, V. M., Villafuerte, C., Bhat, H. S. Rapid tremor migration and pore-pressure waves in subduction zones. Nature Communications, 2018, 9(1): 2900.

Dieterich, J. H. Time-dependent friction and the mechanics of stick-slip. Pure and Applied Geophysics, 1978, 116(4): 790-806.

Ellsworth, W. L. Injection-induced earthquakes. Science, 2013, 341(6142): 1225942.

Eyring, H. The activated complex in chemical reactions. The Journal of Chemical Physics, 1935, 3(2): 107-115.

Feng, W., Yao, L., Cornelio, C., et al. Physical state of water controls friction of gabbro-built faults. Nature Communications, 2023, 14(1): 4612.

Feng, W., Yao, L., Gomila, R., et al. Slip-dependence of fault frictional stability under hydrothermal conditions. Geophysical Research Letters, 2024, 51(14): e2024GL108525.

Gunatilake, T., Miller, S. A. 3-D model reveals thermal decomposition as a potential driver of seismicity in the Apennines, Italy. Geological Society of America Bulletin, 2025, 137(1-2): 341-350.

Hubbert, M., Rubey, W. Role of fluid pressure in mechanics of overthrust faulting: I. Mechanics of fluid-filled porous solids and its application to overthrust faulting. Geological Society of America Bulletin, 1959, 70(2): 115-166.

Hui, G., Chen, Z., Chen, S., et al. Hydraulic fracturing-induced seismicity characterization through coupled modeling of stress and fracture-fault systems. Advances in Geo-Energy Research, 2022, 6(3): 269-270.

Hui, G., Chen, Z., Lei, Z., et al. A synthetical geoengineering approach to evaluate the largest hydraulic fracturing-induced earthquake in the East Shale Basin, Alberta. Petroleum Science, 2023, 20(1): 460-473.

Ikari, M. J., Marone, C., Saffer, D. M., et al. Slip weakening as a mechanism for slow earthquakes. Nature Geoscience, 2013, 6(6): 468-472.

Ito, Y., Hino, R., Kido, M., et al. Episodic slow slip events in the Japan subduction zone before the 2011 Tohoku-Oki earthquake. Tectonophysics, 2013, 600: 14-26.

Jiang, M., Jin, Y., Fu, X., et al. Physical simulation and quantitative characterization of fault zones based on ring-shear experiments. Advances in Geo-Energy Research, 2025, 17(3): 256-266.

Lee, J., Tsai, V. C., Hirth, G., et al. Fault-network geometry influences earthquake frictional behaviour. Nature, 2024, 631(8019): 106-110.

Linker, M. F., Dieterich, J. H. Effects of variable normal stress on rock friction: Observations and constitutive equations. Journal of Geophysical Research: Solid Earth, 1992, 97(B4): 4923-4940.

Liu, J., Zhao, C., Dai, H., et al. Monotonic fluid injection induces fault instability and slip: A laboratory study. Engineering Geology, 2025, 351: 108047.

Luo, Y. D., Ampuero, J. P. Stability of faults with heterogeneous friction properties and effective normal stress. Tectonophysics, 2018, 733: 257-272.

Passelègue, F. X., Almakari, M., Dublanchet, P., et al. Initial effective stress controls the nature of earthquakes. Nature Communications, 2020, 11(1): 5132.

Rao, C. V., Arkin, A. P. Stochastic chemical kinetics and the quasi-steady-state assumption: Application to the Gillespie algorithm. The Journal of Chemical Physics, 2003, 118(11): 4999-5010.

Roche, V., van der Baan, M., Walsh, J. The role of the three-dimensional geometry of fault steps on event migration during fluid-induced seismic sequences. Journal of Geophysical Research: Solid Earth, 2025, 130(2): e2024JB029476.

Ross, Z. E., Cochran, E. S., Trugman, D. T., et al. 3D fault architecture controls the dynamism of earthquake swarms. Science, 2020, 368(6497): 1357-1361.

Ruina, A. Slip instability and state variable friction laws. Journal of Geophysical Research: Solid Earth, 1983, 88(B12): 10359-10370.

Sawai, M., Niemeijer, A. R., Plümper, O., et al. Nucleation of frictional instability caused by fluid pressurization

in subducted blueschist. Geophysical Research Letters, 2016, 43(6): 2543-2551.

Scholz, C. Earthquakes and friction laws. Nature, 1998, 391(6662): 37-42.

Scuderi, M. M., Collettini, C. The role of fluid pressure in induced vs. triggered seismicity: Insights from rock deformation experiments on carbonates. Scientific Reports, 2016, 6(1): 24852.

Scuderi, M. M., Collettini, C. Fluid injection and the mechanics of frictional stability of shale-bearing faults. Journal of Geophysical Research: Solid Earth, 2018, 123(10): 8364-8384.

Scuderi, M. M., Collettini, C., Marone, C. Frictional stability and earthquake triggering during fluid pressure stimulation of an experimental fault. Earth and Planetary Science Letters, 2017, 477: 84-96.

Segall, P., Rice, J. R. Dilatancy, compaction and slip instability of a fluid-infiltrated fault. Journal of Geophysical Research: Solid Earth, 1995, 100(B11): 22155-22171.

Segel, L. A., Slemrod, M. The quasi-steady-state assumption: A case study in perturbation. SIAM Review, 1989, 31(3): 446-477.

Shvarts, A., Yastrebov, V. Trapped fluid in contact interface. Journal of the Mechanics and Physics of Solids, 2018, 119: 140-162.

Sibson, R. H. Arterial faults and their role in mineralizing systems. Geoscience Frontiers, 2019, 10(6): 2093-2100.

Skarbek, R. M., Rempel, A. W., Schmidt, D. A. Geologic heterogeneity can produce aseismic slip transients. Geophysical Research Letters, 2012, 39(21): L21306.

Smith, G. D. Numerical Solution of Partial Differential Equations: Finite Difference Methods. Oxford, UK, Oxford University Press, 1985.

Song, Z., Qian, Y., Mao, Y., et al. Artificial intelligence-based investigation of fault slip induced by stress unloading during geo-energy extraction. Advances in Geo-Energy Research, 2024, 14(2): 106-118.

Sun, Z., Che, M., Zhu, L., et al. Implications for fault reactivation and seismicity induced by hydraulic fracturing. Petroleum Science, 2024, 21(2): 1081-1098.

Sun, Z., Elsworth, D., Cui, G., et al. Impacts of rate of change in effective stress and inertial effects on fault slip behavior: New insights into injection-induced earthquakes. Journal of Geophysical Research: Solid Earth, 2024, 129(2): e2023JB027126.

Tarling, M. S., Smith, S. A., Scott, J. M. Fluid overpressure from chemical reactions in serpentinite within the source region of deep episodic tremor. Nature Geoscience, 2019, 12(12): 1034-1042.

Wang, H. F. Theory of Linear Poroelasticity with Applications to Geomechanics and Hydrogeology. Princeton, USA, Princeton University Press, 2000.

Witherspoon, P. A., Wang, J. S., Iwai, K., et al. Validity of cubic law for fluid flow in a deformable rock fracture. Water Resources Research, 1980, 16(6): 1016-1024.

Yoshida, S., Kato, N. Episodic aseismic slip in a two-degree-of-freedom blockspring model. Geophysical Research Letters, 2003, 30(13): 1681.

Zega, Z., Zhu, W. Stabilizing effect of high pore fluid pressure on fault growth during drained deformation. Journal of Geophysical Research: Solid Earth, 2023, 128(8): e2023JB026536.

Zhang, X., Jeffrey, R. G., Wu, B., et al. Modeling of injection induced seismic events. Paper SPE 181793 Presented at SPE Asia Pacific Hydraulic Fracturing Conference, Beijing, 24-26 August, 2016.

Zhu, J., Kang, J., Elsworth, D., et al. Controlling induced earthquake magnitude by cycled fluid injection. Geophysical Research Letters, 2021, 48(19): e2021GL092885.

Zhu, W., Allison, K. L., Dunham, E. M., et al. Fault valving and pore pressure evolution in simulations of earthquake sequences and aseismic slip. Nature Communications, 2020, 11(1): 4833.